

Electronic structure and transport for nanoscale device simulation

Alex Trellakis and Peter Vogl

Walter-Schottky Institute, Technische Universität München, D-85748 Garching, Germany

1.1 Introduction

Due to the rapid progress in semiconductor manufacturing technology the dimensions of electronic devices are now approaching nanometer-scale, and quantum effects are expected to have an ever increasing influence on electronic properties. For this reason, there is a lot of interest in exploring the ultimate limits of present day semiconductor technology, as exemplified by the 8 nm silicon DGFET shown in Fig. 1.1. Nanoscale MOS devices similar to the one shown are expected to form the foundations of microprocessor technology in the next decade.

But at the same time, quantum effects will eventually become dominant at small-enough length scales and prevent then conventional structures like the one shown from operating. For this reason, is also prudent to start considering completely new devices that operate solely on the basis of these quantum

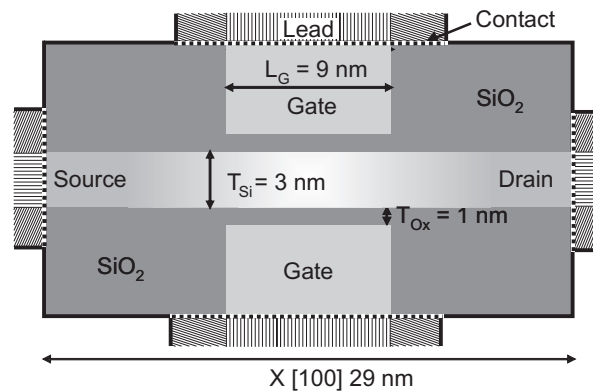


Fig. 1.1. A schematic dual gate MOSFET with a 3 nm wide channel and a 9 nm long gate.

effects, as for instance resonant tunneling diodes or semiconductor Mach-Zehnder interferometers [1]. Furthermore, quantum computing promises computational power that for some purposes like prime factorization surpasses the performance of today's supercomputers by many orders of magnitude.

These reasons are a major incentive for exploring the electronic properties of nanoscale semiconductor devices. Unfortunately, manufacturing a nanodevice and characterizing its electronic behavior is an expensive and time-consuming undertaking in every research setting. For this reason, it is only prudent to use theoretical predictions to guide and explain the experiment. However, even nanostructures like the one shown in Fig. 1.1 contain millions of atoms. This immediately excludes the use of ab-initio methods like density functional theory. But also atomistic approaches like empirical tight binding theory or empirical pseudopotential methods become here quickly unfeasible due to their huge computational effort and their limited generality. Instead, continuum approaches like the k-p-approximation using parameters that are carefully tuned to ab-initio calculations or experiments are used for describing these mesoscopic devices.

For these reasons, state-of-the-art simulators solving continuum equations like the k-p-equations or the drift-diffusion equations have become widely used in the research community. While there are significant differences between these software packages, they all have in common that they solve a simulator-specific set of continuum equations (as for instance the multi-band Schrödinger equation, the Poisson equation, or the drift-diffusion equations) for a wide array of user-definable device structures. This allows the researcher to quickly compare the properties of different devices, or to make predictions for the outcome of experiments. And as long as one is careful enough to remain within the range of validity of the implemented continuum models (this is not always easy!), the results obtained in this fashion should compare quite well to experiment.

This overview focuses on the physical models that are used for the simulation of electronic states and currents in nanostructures. Therefore, much of the material presented here can also be found in text books for solid-state theory like [2]. In specific, part 1 starts out with a short discussion of the origin of band structures in crystalline solids and presents the k-p-equations. Here, we will also discuss a few models for the conduction and valence bands in semiconductors. In part 2, we present the envelope function approximation for heterostructures and consider the effects of elastic deformations and strain. Furthermore, we also examine carrier densities and effects of doping at non-zero temperature and consider the interplay of the Poisson and Schrödinger equation. In part 3, we present the Boltzmann equation as semi-classical transport model, and discuss the merits of drift-diffusion as a more practical alternative for larger devices. We also show how to add quantum corrections for size quantization to drift-diffusion and consider ballistic quantum transport. Finally, in part 4 we present **nextnano**³, a software package for the simulation of nanostructures that has been developed by the authors [3]. Here, we give a

short overview of the simulator's capabilities and the numerical methods that it uses, and present an example application.

1.2 Electronic structure of semiconductors

1.2.1 Bloch theory and the band structure

Essentially all semiconductors used today are based on crystalline materials, where all constituent ions or atoms, or electronic charges are arranged in a periodic lattice. Consequently, every crystal is invariant under translations $T(\mathbf{R})$ defined by the discrete set of translation vectors

$$\mathbf{R} = n_1 \mathbf{a}_1 + n_2 \mathbf{a}_2 + n_3 \mathbf{a}_3 \quad , n_1, n_2, n_3 \in \mathbb{Z} \quad (1.1)$$

where the three vectors $\mathbf{a}_1, \mathbf{a}_2, \mathbf{a}_3$ define the primitive cell of the crystal lattice. Furthermore, all crystal lattices are also invariant under some point operations as inversion or rotation by $60^\circ, 90^\circ$, or 180° , where the exact symmetry group directly depends on the properties of the underlying crystal lattice.

We now make the simplifying assumption that only the outermost electrons of each atom contribute significantly to the electronic properties of the crystal, while the nuclei and the inner shell electrons form a static external ion potential

$$V_{\text{ion}}(\mathbf{x} + \mathbf{R}) = V_{\text{ion}}(\mathbf{x}) \quad (1.2)$$

that is periodic for all lattice vectors \mathbf{R} . In this case, the resulting many-body Hamiltonian for the outer shell electrons becomes excluding spin effects

$$\hat{H} = \sum_i \left[\frac{\hat{\mathbf{p}}_i^2}{2m} + V_{\text{ion}}(\hat{\mathbf{x}}_i) \right] + \frac{1}{2} \sum_{i \neq j} \frac{e^2}{|\hat{\mathbf{x}}_i - \hat{\mathbf{x}}_j|} \quad (1.3)$$

where the last term describes the Coulomb repulsion between the electrons.

Unfortunately, the resulting N -fermion Schrödinger equation is much too complex for an exact solution without additional simplifications. For instance, in density functional theory one replaces \hat{H} by a carefully constructed one-body Hamiltonian

$$\hat{H}_1 = \frac{\hat{\mathbf{P}}^2}{2m} + V_{\text{ion}}(\hat{\mathbf{x}}) + V[n](\hat{\mathbf{x}}) \quad (1.4)$$

with an additional one-body potential $V[n](\mathbf{x})$. This extra potential depends self-consistently on the ground-state electron density of \hat{H}_1

$$n(\mathbf{x}) = \sum_{E_n < E_F} |\Psi_n(\mathbf{x})|^2 \quad (1.5)$$

where the sum runs over all occupied energy levels E_n below the Fermi energy E_F .

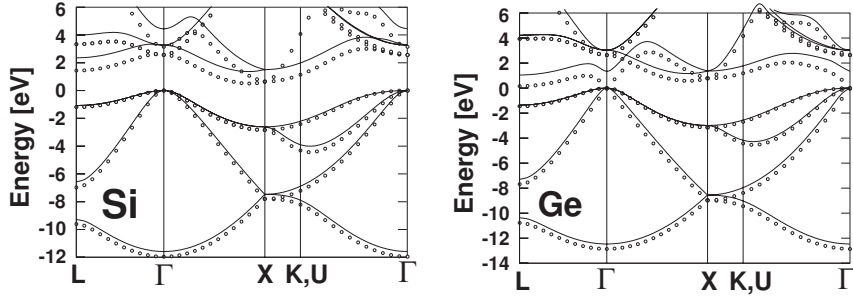


Fig. 1.2. Band structures for Si and Ge calculated with two variants of the density functional method. Open circles denote results for the LDA approximation and the solid line results from the more accurate EXX method (after [4]).

One can show now that also $V[n](\hat{\mathbf{x}})$ is periodic with respect to all lattice vectors \mathbf{R} . Consequently, due to Bloch's theorem all eigenstates of \hat{H}_1 must have the form

$$\hat{\Psi}_{n,\mathbf{k}}(\mathbf{x}) = e^{i\mathbf{k}\cdot\mathbf{x}} u_{n,\mathbf{k}}(\mathbf{x}) \quad (1.6)$$

with

$$u_{n,\mathbf{k}}(\mathbf{x} + \mathbf{R}) = u_{n,\mathbf{k}}(\mathbf{x}) \quad (1.7)$$

Furthermore, we also get that the Bloch factors $u_{n,\mathbf{k}}(\mathbf{x})$ obey

$$E_n(\mathbf{k}) u_{n,\mathbf{k}}(\mathbf{x}) = \hat{H}(\mathbf{k}) u_{n,\mathbf{k}}(\mathbf{x}) \quad (1.8)$$

$$= \left[\frac{(\hat{\mathbf{p}} + \hbar\mathbf{k})^2}{2m_0} + \hat{V}_{\text{ion}} + \hat{V}[n] \right] u_{n,\mathbf{k}}(\mathbf{x}) \quad (1.9)$$

where the energy surfaces in reciprocal space $E_n(\mathbf{k})$ are also called the band structure of the semiconductor (Fig. 1.2).

1.2.2 The $\mathbf{k}\cdot\mathbf{p}$ -approximation

However, most properties of semiconductors that are experimentally accessible depend only the position and shape of the minima and maxima \mathbf{k}_0 of the conduction and valence bands, and a precise knowledge of the entire band structure is not needed. For this reason, we now expand $E_n(\mathbf{k})$ around these extrema \mathbf{k}_0 and rewrite the Hamiltonian as

$$\hat{H}(\mathbf{k}) = \hat{H}(\mathbf{k}_0) + \frac{\hbar}{m_0} (\mathbf{k} - \mathbf{k}_0) \cdot \hat{\mathbf{p}} + \frac{\hbar^2}{2m_0} (\mathbf{k} - \mathbf{k}_0)^2 \quad (1.10)$$

with eigenfunctions

$$\hat{H}(\mathbf{k}_0) u_{n,\mathbf{k}_0}(\mathbf{x}) \equiv \left[\frac{(\hat{\mathbf{p}} + \hbar \mathbf{k}_0)^2}{2m_0} + \hat{V}_{\text{ion}} + \hat{V}[n] \right] u_{n,\mathbf{k}_0}(\mathbf{x}) \quad (1.11)$$

$$= E_n(\mathbf{k}_0) u_{n,\mathbf{k}_0}(\mathbf{x}) \quad (1.12)$$

Next, we use that the Bloch factors $u_{n,\mathbf{k}}(\mathbf{x})$ form a complete set of basis functions for every \mathbf{k} and in specific also for \mathbf{k}_0 . Therefore, we may insert the expansion

$$u_{n,\mathbf{k}}(\mathbf{x}) = \sum_{\alpha} c_{n,\alpha}(\mathbf{k}) u_{\alpha,\mathbf{k}_0}(\mathbf{x}) \quad (1.13)$$

into Schrödinger's equation (1.8) and get after a short calculation the set of equations

$$E_n(\mathbf{k}) c_{n,\alpha}(\mathbf{k}) = \sum_{\beta} H_{\alpha\beta}(\mathbf{k}) c_{n,\beta}(\mathbf{k})$$

with a Hamilton matrix

$$H_{\alpha\beta}(\mathbf{k}) = \left[E_{\beta}(\mathbf{k}_0) + \frac{\hbar^2}{2m_0} (\mathbf{k} - \mathbf{k}_0)^2 \right] \delta_{\alpha\beta} + \frac{\hbar}{m_0} (\mathbf{k} - \mathbf{k}_0) \cdot \mathbf{p}_{\alpha\beta} \quad (1.14)$$

that contains momentum matrix elements

$$\mathbf{p}_{\alpha\beta} = \int u_{\alpha,\mathbf{k}_0}^*(\mathbf{x}) \hat{\mathbf{p}} u_{\beta,\mathbf{k}_0}(\mathbf{x}) d^3x \quad (1.15)$$

As the next step, we separate the energy bands into two groups A and B [5], where A contains a few bands of interest near the Fermi energy E_F and B all remaining bands. Using the so-called k-p-approximation, we now assume that the non-diagonal coupling term

$$\frac{\hbar}{m_0} (\mathbf{k} - \mathbf{k}_0) \cdot \mathbf{p}_{\alpha\beta} \quad (1.16)$$

in (1.14) is weak between states from A and B and can be treated as a perturbation [6, 7, 8, 9]. In this case, the Hamilton matrix from (1.14) now becomes the k-p-matrix

$$H_{\alpha\beta}(\mathbf{k}) = \left[E_{\alpha}(\mathbf{k}_0) + \frac{\hbar^2 (\mathbf{k} - \mathbf{k}_0)^2}{2m_0} \right] \delta_{\alpha\beta} + \frac{\hbar}{m_0} (\mathbf{k} - \mathbf{k}_0) \cdot \mathbf{p}_{\alpha\beta} + \sum_{\gamma \in B} \frac{\hat{H}_{\alpha\gamma}(\mathbf{k}) \hat{H}_{\gamma\beta}(\mathbf{k})}{E_{\alpha}(\mathbf{k}_0) - E_{\gamma\gamma}(\mathbf{k})} \quad (1.17)$$

where both indices α and β now belong to group A .

Note that the momentum matrix elements $\mathbf{p}_{\alpha\beta}$ in this expression can also be used as fitting parameters in order to match experimentally obtained results, as long one takes into account that many of the $\mathbf{p}_{\alpha\beta}$ vanish due to symmetry considerations.

1.2.3 Conduction and valence band models

At this point we need to decide how many bands need to be placed in group A in order to get sufficiently accurate results. For instance, if we place only one band n into group A , we get the so-called effective mass approximation, and the k-p-approximation yields

$$H_{\text{eff}}(\mathbf{k}) = E_n(\mathbf{k}_0) + \frac{\hbar^2 (\mathbf{k} - \mathbf{k}_0)^2}{2m_0} + \frac{\hbar^2}{m_0^2} \sum_{n' \neq n} \frac{|\mathbf{P}_{nn'}|^2}{E_n(\mathbf{k}_0) - E_{n'}(\mathbf{k}_0)} \quad (1.18)$$

$$\equiv E_n(\mathbf{k}_0) + \frac{\hbar^2}{2} \sum_{i,j=1}^3 \left(\frac{1}{m^*} \right)_{ij} (k_i - k_{0,i})(k_j - k_{0,j}) \quad (1.19)$$

where the symmetric 3×3 -matrix m^* is also called the effective mass of the electron.

While the effective mass approximation often suffices for the description of the conduction band, the valence bands are created by the p -orbitals in most semiconductors and are therefore threefold degenerate. For this reason, a k-p-model for the valence bands needs to include at least three bands in the orbital basis

$$|x_1\rangle, |x_2\rangle, |x_3\rangle \quad (1.20)$$

which for Zincblende materials at the Γ -point like GaAs then results into a k-p-Hamiltonian [10]

$$H_{\alpha\beta}^{3 \times 3}(\mathbf{k}) = E_\alpha(\mathbf{0}) + \frac{\hbar^2}{2m_0} \mathbf{k}^2 + N \mathbf{k} \mathbf{k}^T + (L - N) \text{diag}(k_1^2, k_2^2, k_3^2) \quad (1.21)$$

$$+ M \text{diag}(k_2^2 + k_3^2, k_1^2 + k_3^2, k_1^2 + k_2^2) \quad (1.22)$$

The parameters L, M, N here are also called the Dresselhaus parameters [7] and depend as m^* on the momentum matrix elements $\mathbf{p}_{\alpha\beta}$. In a similar fashion, we can include even more bands into the k-p-Hamiltonian (as for instance the conduction band) in order to achieve a yet more accurate band structure model.

But an accurate description of the valence bands also requires the inclusion of spin effects. Therefore, we modify our orbital basis for the valence bands as

$$|x_1 \uparrow\rangle, |x_2 \uparrow\rangle, |x_3 \uparrow\rangle, |x_1 \downarrow\rangle, |x_2 \downarrow\rangle, |x_3 \downarrow\rangle \quad (1.23)$$

and get a degenerate 6×6 -Hamilton matrix

$$H_{6 \times 6}(\mathbf{k}) = \begin{pmatrix} H^{3 \times 3}(\mathbf{k}) & 0 \\ 0 & H^{3 \times 3}(\mathbf{k}) \end{pmatrix} \quad (1.24)$$

with $H^{3 \times 3}(\mathbf{k})$ being defined as above. This degeneracy is then partially lifted by the addition of a spin-orbit coupling term $H_{\text{so}}^{6 \times 6}$, which results into the lowering of the split-off hole band shown in Fig. 1.3.

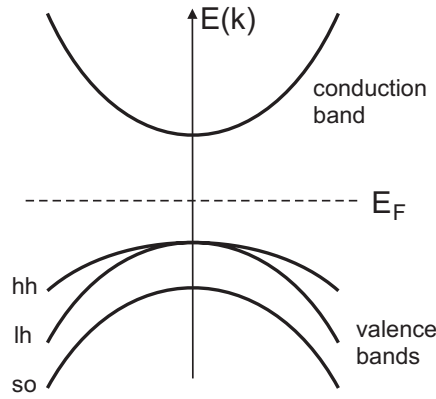


Fig. 1.3. The band structure near the Γ -point for a direct band gap semiconductor like GaAs. Shown are the conduction band, the heavy hole (hh), light hole (lh), and the split-off hole (so) valence bands, and the Fermi level E_F .

1.3 Heterostructures

1.3.1 The envelope function approximation

Until now we have only considered perfectly periodic infinite-size semiconductor crystals. However, realistic nanostructures not only have a very small finite size, but they may also contain variations in material composition and be subjected to non-uniform external potentials $V_{\text{ext}}(\mathbf{x})$. As a consequence, the Hamiltonian describing these systems is not translation invariant and neither Bloch's theorem nor equation (1.8) for the Bloch factors is available.

Fortunately, for many structures it is possible to use the envelope function approximation [6] in order to obtain results. For this approximation, we assume that a semiconductor with homogeneous material composition is subjected to an external potential $V_{\text{ext}}(\mathbf{x})$. In this case, we can write the wave function $\psi(\mathbf{x})$ as a superposition of Bloch factors with position dependent weight factors $F_\alpha(\mathbf{x})$ called envelope functions as

$$\Psi(\mathbf{x}) = \sum_{\alpha \in A} F_\alpha(\mathbf{x}) u_{\alpha, \mathbf{k}_0}(\mathbf{x}) \quad (1.25)$$

where the sum runs again over all bands A included in our k-p-model. If we now assume that $V_{\text{ext}}(\mathbf{x})$ varies only slowly with respect to the lattice constant, we may substitute the wave vector by the momentum operator as

$$\mathbf{k} - \mathbf{k}_0 \longrightarrow \hat{\mathbf{p}} = \frac{\hbar}{i} \nabla \quad (1.26)$$

in our effective mass or k-p-Hamiltonian in order to obtain a real-space Hamiltonian for the envelope function $F_\alpha(\mathbf{x})$. For example, in the effective mass

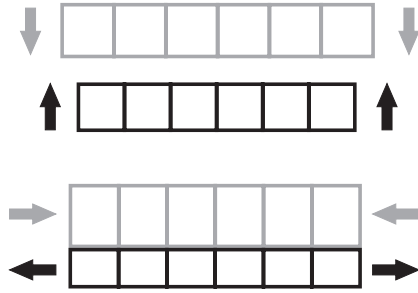


Fig. 1.4. A schematic illustration for strain effects in lattice matched heterostructures. Note that a compression in one direction is always accompanied by an expansion in the other direction and vice versa.

approximation discussed earlier we then get for the conduction band edge E_C the simple Hamiltonian

$$H_{\text{eff}}(\hat{\mathbf{p}}) = \frac{1}{2} \hat{\mathbf{p}} \cdot \left(\frac{1}{m^*} \hat{\mathbf{p}} \right) + E_C(\mathbf{k}_0) + V_{\text{ext}}(\hat{\mathbf{x}}) \quad (1.27)$$

where we have taken into account that the effective mass m^* is actually a 3×3 -matrix.

Incidentally, this approach is also widely used for the simulation of heterostructures, even though there the material composition is not constant but changes abruptly at the material interfaces (see [11, 12] for a justification). For example, in the effective mass approximation one usually makes the mass tensor m^* and the conduction band edge E_C position-dependent and uses the Hamiltonian

$$H_{\text{eff}}(\hat{\mathbf{p}}) = \frac{1}{2} \hat{\mathbf{p}} \cdot \left[\frac{1}{m^*(\hat{\mathbf{x}})} \hat{\mathbf{p}} \right] + E_C(\hat{\mathbf{x}}, \mathbf{k}_0) + V_{\text{ext}}(\hat{\mathbf{x}}) \quad (1.28)$$

in order to get quite accurate results. Similarly, we can also make all parameters in the multi-band k-p-Hamiltonians $H_{A \times A}(\hat{\mathbf{p}})$ position-dependent and obtain satisfactory results, as long as all operator ordering issues are properly taken into account.

1.3.2 Elastic deformation and strain

Another important physical effect that needs to be considered in the context of heterostructures are elastic deformations and therefore strain. For example, let us consider the situation where two materials with similar crystal structure but different lattice constants are epitaxially grown onto each other, as shown in Fig. 1.4. We immediately see that the crystal lattices need to compress or expand in the growth plane in order to achieve coherent growth with mutually

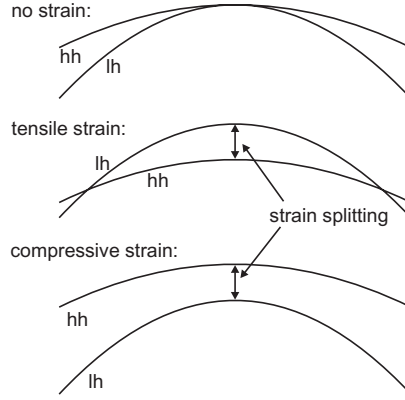


Fig. 1.5. The effects of strain on the valence bands in GaAs for different types of strain.

matching chemical bonds. At the same time, we also note that every compression in the growth plane is accompanied by a corresponding expansion in the other directions and vice versa.

The elastic deformations that occur in all these cases are usually described by a displacement vector

$$\mathbf{u}(\mathbf{x}) = \mathbf{x}'(\mathbf{x}) - \mathbf{x} \quad (1.29)$$

where \mathbf{x} and \mathbf{x}' are the positions of each mass point before and after the deformation. These deformations then results into a strain that for the typically small displacements in a semiconductor is given by the strain tensor

$$\varepsilon_{ij}(\mathbf{x}) = \frac{1}{2} [\partial_i u_j(\mathbf{x}) + \partial_j u_i(\mathbf{x})] \quad (1.30)$$

Using perturbation theory [13] one can show now that the band structure is modified in the presence of strain. In specific, we find that strain shifts the conduction band by an amount

$$E_c \longrightarrow E_c + a_c \text{Tr}(\varepsilon) \quad (1.31)$$

where the constant a_c is also called the absolute deformation potential. The influence of strain on the valence band is given by an additional term

$$H_{\alpha\beta}^{3 \times 3}(\mathbf{k}) \longrightarrow H_{\alpha\beta}^{3 \times 3}(\mathbf{k}) + S_{\alpha\beta}(\varepsilon) \quad (1.32)$$

in the k-p-matrix with

$$S_{\alpha\beta} = \begin{pmatrix} l\varepsilon_{11} + m(\varepsilon_{22} + \varepsilon_{33}) & n\varepsilon_{12} & n\varepsilon_{13} \\ n\varepsilon_{12} & l\varepsilon_{22} + m(\varepsilon_{11} + \varepsilon_{33}) & n\varepsilon_{23} \\ n\varepsilon_{13} & n\varepsilon_{23} & l\varepsilon_{33} + m(\varepsilon_{11} + \varepsilon_{22}) \end{pmatrix} \quad (1.33)$$

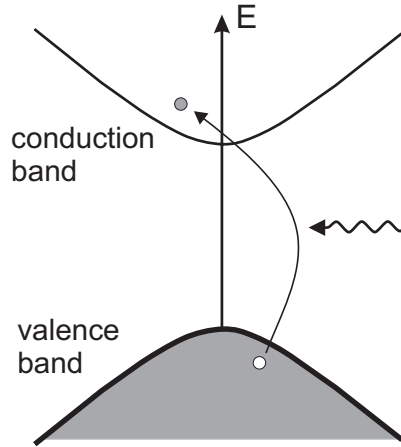


Fig. 1.6. An electron is excited from a valence band to the conduction band, leaving a hole at its original place.

where the parameters l, m, n are connected to the absolute deformation potential of the valence band a_v and its shear deformation potentials b, d by

$$l = a_v + 2b \quad m = a_v - b \quad n = \sqrt{3}d \quad (1.34)$$

Thus we find here that strain can lift the degeneracy between light holes and heavy holes in the valence band as shown in Fig. 1.5.

1.3.3 Carrier densities at non-zero temperature

So far we have ignored the effects of a non-zero temperature in semiconductor structures. At zero temperature and in absence of external electromagnetic fields, the conduction band is devoid of electrons while the valence bands are completely occupied due to the Fermi energy E_F being between both band edges as

$$E_V < E_F < E_C \quad (1.35)$$

Consequently, neither band can carry an electric current and the semiconductor becomes an insulator.

For non-zero temperatures this situation changes significantly. Now we find that sufficiently energetic lattice vibrations (or phonons) can lift electrons from a valence band into the conduction band, while leaving a positively charged hole in the valence band behind (see Fig.1.6), a process that is also called (pair) generation. These excess electrons and the holes can now be easily accelerated by electromagnetic fields, which can lead to a buildup of space charges and the presence of electric currents. Finally, an electron-hole

pair may also recombine under the emission of a phonon or photon, with the electron filling up the gap that originally belonged to the hole.

In thermal equilibrium, the generation and recombination processes balance each other and the occupation $N_e(E)$ for a state with energy E is given by the Fermi distribution as

$$N_e(E) = \frac{2}{1 + \exp\left(\frac{E - E_F}{k_B T}\right)} \quad (1.36)$$

where k_B is the Boltzmann constant and T the temperature of the system. If we now use a suitable envelope function Hamiltonian \hat{H}_C in order to determine the wave functions of the conduction band electrons

$$\hat{H}_C \psi_n^e(\mathbf{x}) = E_n^e \psi_n^e(\mathbf{x}) \quad (1.37)$$

we then get for the corresponding electron density

$$n(\mathbf{x}) = \sum_n N_e(E_n^e) |\psi_n^e(\mathbf{x})|^2 \quad (1.38)$$

At the same time, the occupation $N_h(E)$ of a hole state at energy E in a valence band is given by a Fermi distribution as well with

$$N_h(E) = \frac{2}{1 + \exp\left(\frac{E_F - E}{k_B T}\right)} \quad (1.39)$$

Therefore, starting from a suitable k·p-Hamiltonian \hat{H}_V for the valence bands with

$$\hat{H}_V \psi_n^h(\mathbf{x}) = E_n^h \psi_n^h(\mathbf{x}) \quad (1.40)$$

we now get as expected

$$p(\mathbf{x}) = \sum_n N_h(E_n^h) |\psi_n^h(\mathbf{x})|^2 \quad (1.41)$$

for the hole density.

The number of free carriers in a semiconductor is further modified by the presence of dopant atoms. Here, electron donors require a small ionization energy E_d to donate an electron to the conduction band, while electron acceptors need a small energy E_a to remove an electron from the valence band and create a hole in its place. The ionization energies E_d and E_a are small compared to the band gap for both kind of species, which results in the dopant atoms to be mostly ionized at room temperature. As a result, electron donors lead to a massive increase of the electron density (and a corresponding decrease in the hole density), while electron acceptors result in a large decrease of the hole density (and a corresponding decrease in the electron density). Finally, as a side effect of their almost complete ionization at room temperature dopants also result in a positive space charge $N_D^+(\mathbf{x})$ in the case of donors and a negative space charge $N_A^-(\mathbf{x})$ in the case of acceptors.

1.3.4 Charge distributions and the Poisson equation

All these space charges together with the free electrons and holes and possible surface charges $\rho_s(\mathbf{x})$ add up to a total charge

$$\rho(\mathbf{x}) = e [p(\mathbf{x}) - n(\mathbf{x}) + N_D^+(\mathbf{x}) - N_A^-(\mathbf{x}) + \rho_s(\mathbf{x})] \quad (1.42)$$

that can be quite large at some places. As a result, we get according to Poisson's equation

$$\nabla \cdot [\epsilon(\mathbf{x}) \nabla \phi(\mathbf{x})] = -\rho(\mathbf{x}) \quad (1.43)$$

an electric potential $\phi(\mathbf{x})$ that warps the conduction and valence band edges E_C and E_V as

$$E_C \longrightarrow E_C[\phi] = E_C - e\phi \quad (1.44)$$

$$E_V \longrightarrow E_V[\phi] = E_V - e\phi \quad (1.45)$$

As consequence, both the carrier densities and the ionized dopant space charges become potential-dependent, and the Poisson equation (1.43) now becomes nonlinear in the electrostatic potential ϕ as

$$\nabla \cdot (\epsilon \nabla \phi) = -e (p[\phi] - n[\phi] + N_D^+[\phi] - N_A^-[\phi] + \rho_s) \quad (1.46)$$

Here, the dependence of the carrier densities n and p on ϕ is a consequence of $E_C[\phi]$ and $E_V[\phi]$ entering the Hamiltonian in Schrödinger's equation as

$$\hat{H}_C \longrightarrow \hat{H}_C[\phi] = \hat{H}_C - e\hat{\phi} \quad (1.47)$$

$$\hat{H}_V \longrightarrow \hat{H}_V[\phi] = \hat{H}_V - e\hat{\phi} \quad (1.48)$$

which then of course makes also the electron and hole wave functions and their energies ϕ -dependent as

$$\psi_n^e = \psi_n^e[\phi] \quad E_n^e = E_n^e[\phi] \quad (1.49)$$

$$\psi_n^h = \psi_n^h[\phi] \quad E_n^h = E_n^h[\phi] \quad (1.50)$$

Therefore, we not only need to solve a nonlinear Poisson equation (1.46) for ϕ , we also need to solve (1.46) together with the Schrödinger equation in order to obtain a correct self-consistent set of quantum states and carrier densities.

1.4 Carrier transport in nanostructures

1.4.1 Classical ballistic transport

The reader might have noticed that in the last section about heterostructures we have assumed thermal equilibrium with a position independent temperature T and Fermi level E_F . But of course all semiconductor devices like the

one shown in Fig. 1.1 have at least two contacts where an external bias can be applied. If the applied bias is not the same for all contacts, we immediately get a non-equilibrium situation where electrical currents flow and the carrier distributions may become time-dependent.

Developing an accurate quantum transport theory for these systems now requires the additional inclusion of phonons to the many-body Schrödinger equation describing the physical system. A model that can be employed for this type of system is for instance the non-equilibrium Green's function approach (see [14] and the text books [15, 16] for in-depth expositions).

But we can already achieve a first understanding of carrier transport by starting out with a classical ballistic transport model, where we assume that all carriers move as compact uncertainty-limited wave packets along classical orbits $\mathbf{x}(t)$ and $\mathbf{k}(t)$ in phase space. These classical orbits obey for a single energy band $E(\mathbf{k})$ the equations

$$\dot{\mathbf{x}} = \frac{1}{\hbar} \nabla_{\mathbf{k}} E(\mathbf{k}) \quad (1.51)$$

$$\hbar \dot{\mathbf{k}} = q \mathbf{E}(\mathbf{x}, t) \quad (1.52)$$

where the second equation is the electrostatic force on a particle with charge q .

As we have discussed earlier, $E(\mathbf{k})$ is periodic in reciprocal space but can be approximated near a minimum \mathbf{k}_0 by

$$E(\mathbf{k}) \approx \frac{\hbar^2}{2} (\mathbf{k} - \mathbf{k}_0) \cdot \left[\frac{1}{m^*} (\mathbf{k} - \mathbf{k}_0) \right] \quad (1.53)$$

which then leads to a simplified equation of motion

$$\dot{\mathbf{x}} = \frac{\hbar}{m^*} (\mathbf{k} - \mathbf{k}_0) \quad (1.54)$$

or

$$m^* \ddot{\mathbf{x}} = q \mathbf{E}(\mathbf{r}, t) \quad (1.55)$$

which is the Newton force law for an anisotropic mass tensor m^* .

1.4.2 Scattering and the Boltzmann equation

We now add carrier-phonon scattering as discrete events in time where a carrier wave packet undergoes an instantaneous transition from a reciprocal space point \mathbf{k} to another \mathbf{k}' . The transition probability $S(\mathbf{k}, \mathbf{k}')$ for these scattering events derives of course from quantum mechanics and is accompanied by a phase change $\delta\varphi$ which we assume to be random for simplicity.

The inelastic mean free path between these scattering events (and therefore also the coherence length) now varies for different semiconductors and scattering mechanisms typically between about 3 and 100 nm which is much

larger than a single lattice constant. This justifies the use of a band structure $E(\mathbf{k})$ between scattering events.

At the same time, the size of the wave packet in phase space needs to obey the uncertainty relation

$$\Delta x \Delta k \approx 1 \quad (1.56)$$

where the upper limit for Δx is given by the coherence length and the one for Δk by the Brillouin zone boundary at

$$k_{\max} \approx 10^{10} \text{ m}^{-1} \quad (1.57)$$

If we now choose Δx matching to the coherence length as

$$\Delta x \approx 10 - 100 \text{ nm} \quad (1.58)$$

we get from (1.56)

$$\Delta k \approx 10^7 - 10^8 \text{ m}^{-1} \ll k_{\max} \quad (1.59)$$

which is sufficiently accurate to sample reciprocal space. Therefore, as long as we do not attempt to localize the particle in phase space with higher accuracy as given by the pair Δx and Δk , we can define a distribution function $f(\mathbf{x}, \mathbf{k}, t)$ that represents the probability to find the particle between the phase space points (\mathbf{x}, \mathbf{k}) and $(\mathbf{x} + d\mathbf{x}, \mathbf{k} + d\mathbf{k})$.

Flux conservation in phase space due to Liouville's theorem gives us now immediately the Boltzmann equation

$$\frac{df}{dt} \equiv \frac{\partial f}{\partial t} + \dot{\mathbf{x}} \cdot \nabla_{\mathbf{x}} f + \dot{\mathbf{k}} \cdot \nabla_{\mathbf{k}} f \quad (1.60)$$

$$= \frac{\partial f}{\partial t} + \frac{1}{\hbar} \nabla_{\mathbf{k}} E(\mathbf{k}) \cdot \nabla_{\mathbf{x}} f + \frac{q}{\hbar} \mathbf{E}(\mathbf{x}, t) \cdot \nabla_{\mathbf{k}} f = \left. \frac{df}{dt} \right|_{\text{scatt}} \quad (1.61)$$

where we have collected all variations in f due to scattering in the term at the right. For this scattering term one can easily show that it must be equal to

$$\left. \frac{df(\mathbf{x}, \mathbf{k}, t)}{dt} \right|_{\text{scatt}} = \int d^3 k' f(\mathbf{x}, \mathbf{k}', t) S(\mathbf{k}', \mathbf{k}) [1 - f(\mathbf{x}, \mathbf{k}, t)] \quad (1.62)$$

$$- \int d^3 k' f(\mathbf{x}, \mathbf{k}, t) S(\mathbf{k}, \mathbf{k}') [1 - f(\mathbf{x}, \mathbf{k}', t)] \quad (1.63)$$

where the integrals run over the entire first Brillouin zone, and the factors $1 - f$ are a direct consequence of the Pauli exclusion principle.

The Boltzmann equation as presented in (1.61) is a time-dependent six-dimensional integro-differential equation that due to its complexity cannot be solved accurately (even though approximate solutions obtained using Monte Carlo methods suffice for some applications). This situation is aggravated by the fact that the (now classical) electron density

$$n(\mathbf{x}) = \int d^3k f(\mathbf{x}, \mathbf{k}, t) \quad (1.64)$$

is a source term in Poisson's equation (1.43). Since the gradient of the electrostatic potential ϕ enters the Boltzmann equation (1.61) via $\mathbf{E} = -\nabla\phi$, a self-consistent solution of both partial differential equations is required.

In addition, if both electrons and holes are present we need two phase space densities f_n and f_p that each obey their own Boltzmann equation with different band structures $E_n(\mathbf{k})$ and $E_p(\mathbf{k})$. These two equations couple then directly through pair generation and recombination and indirectly through $\nabla\phi$ from Poisson's equation (1.43).

Finally, it is important to emphasize that the size of most nanostructures is comparable or smaller than the 10 – 100 nm we have assumed earlier for Δx . Therefore, some quantum corrections to the Boltzmann equation (1.61) are needed in order to obtain reasonable results.

1.4.3 The drift-diffusion equations

For semiconductor devices that are large enough compared to Δx we can often replace Boltzmann's equation by the much simpler drift-diffusion equations. For this drift-diffusion model, we assume that the electric fields \mathbf{E} are small enough and the scattering events frequent enough that the system is locally at each point \mathbf{x} almost in thermal equilibrium. With other words, we assume that the phase space distributions f_n and f_p are approximately Fermi distributed in \mathbf{k} -space for each \mathbf{x} , with quasi-Fermi levels $E_{F,n}(\mathbf{x}, t)$ and $E_{F,p}(\mathbf{x}, t)$ that are now position-dependent. In this case, we get for the electron and hole density in quasi-equilibrium

$$n(\mathbf{x}, t) = \int_0^\infty dE \frac{g_C(E)}{1 + \exp\left[\frac{E_C(\mathbf{x}, t) - E_{F,n}(\mathbf{x}, t) + E}{k_B T}\right]} \quad (1.65)$$

$$p(\mathbf{x}, t) = \int_0^\infty dE \frac{g_V(E)}{1 + \exp\left[\frac{E_{F,p}(\mathbf{x}, t) - E_V(\mathbf{x}, t) + E}{k_B T}\right]} \quad (1.66)$$

where $E_C(\mathbf{x})$ and $E_V(\mathbf{x})$ are the conduction and valence band edges, and $g_C(E)$ and $g_V(E)$ the density-of-states for electrons and holes.

Furthermore, since the electron and hole phase space densities f_n and f_p deviate only slightly from the Fermi distribution in \mathbf{k} -space, we can make a moment expansion which then yields in zeroth order the following continuity equations for electrons and holes

$$\frac{\partial n(\mathbf{x}, t)}{\partial t} + \nabla \cdot \mathbf{j}_n(\mathbf{x}, t) = G(\mathbf{x}, t) - R(\mathbf{x}, t) \quad (1.67)$$

$$\frac{\partial p(\mathbf{x}, t)}{\partial t} + \nabla \cdot \mathbf{j}_p(\mathbf{x}, t) = G(\mathbf{x}, t) - R(\mathbf{x}, t) \quad (1.68)$$

where \mathbf{j}_n and \mathbf{j}_p are the electrons and hole particle currents and G and R the pair generation and recombination rates. The currents themselves are given by the first order component of the moment expansion as

$$\mathbf{j}_n(\mathbf{x}, t) = -\mu_n(\mathbf{x}) n(\mathbf{x}, t) \nabla E_{F,n}(\mathbf{x}, t) \quad (1.69)$$

$$\mathbf{j}_p(\mathbf{x}, t) = \mu_p(\mathbf{x}) p(\mathbf{x}, t) \nabla E_{F,p}(\mathbf{x}, t) \quad (1.70)$$

where $\mu_n(\mathbf{x})$ and $\mu_p(\mathbf{x})$ are the electron and hole mobilities.

This set of equations (1.67-1.70) are called the drift-diffusion equations, and form together with the Poisson equation (1.43) the basis of many commercially available semiconductor device simulators. The accuracy of the drift-diffusion approximation can be further improved by using complicated phenomenological models for the carrier mobilities and generation and recombination rates. Furthermore, non-uniform carrier temperatures and heat transport can also be included if needed. Especially the commercially available simulators offer here many options for silicon based MOS transistors.

1.4.4 Quantum corrected drift-diffusion

But as we have seen earlier, for nanoscale semiconductor structures quantum mechanics will lead to major deviations from the Boltzmann equation and therefore also from the drift-diffusion equations. Luckily enough, there are important mesoscopic structures like the DGFET shown in Fig. 1.1 where quantum mechanical size quantization must be included but no ballistic transport or resonant tunneling takes place. For such physical systems, a quantum correction to the *stationary* drift-diffusion equations is still possible and a full quantum transport calculation can be avoided [17, 18].

The key to finding this quantum correction lies in the realization that the electron and hole densities in (1.67-1.70) are purely classical and can therefore not take into account size quantization. We can correct this deficiency by using the electron and hole Hamiltonians $\hat{H}_C[\phi]$ and $\hat{H}_V[\phi]$ for calculating the electron and hole envelope wave functions as

$$\hat{H}_C[\phi] \psi_n^e(\mathbf{x}) = E_n^e \psi_n^e(\mathbf{x}) \quad (1.71)$$

$$\hat{H}_V[\phi] \psi_n^h(\mathbf{x}) = E_n^h \psi_n^h(\mathbf{x}) \quad (1.72)$$

and then determining the corresponding carrier densities through the electron and hole Fermi levels $E_{F,n}(\mathbf{x})$ and $E_{F,p}(\mathbf{x})$ using formulas (1.36-1.41) as

$$n(\mathbf{x}) = 2 \sum_n \frac{|\psi_n^e(\mathbf{x})|^2}{1 + \exp\left(\frac{E_n^e - E_{F,n}(\mathbf{x})}{k_B T}\right)} \quad (1.73)$$

and

$$p(\mathbf{x}) = 2 \sum_n \frac{|\psi_n^h(\mathbf{x})|^2}{1 + \exp\left(\frac{E_{F,p}(\mathbf{x}) - E_n^h}{k_B T}\right)} \quad (1.74)$$

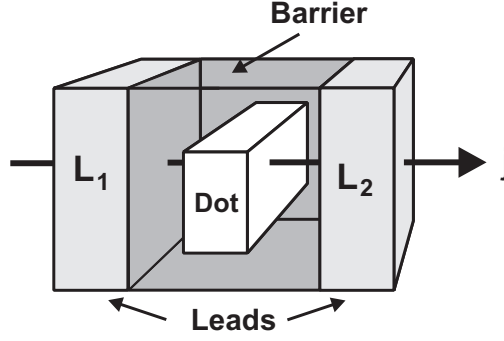


Fig. 1.7. A model quantum dot resonant tunneling structure. The quantum dot has the dimensions $14 \times 14 \times 5$ nm and is embedded in a 15 nm thick barrier region (after [20]).

where we have implicitly also used the adiabatic approximation for the wave function.

These quantum densities can now be entered into the drift-diffusion equations (1.67-1.70) which for stationary currents become with

$$\nabla \cdot \mathbf{j}_n(\mathbf{x}) = -\nabla \cdot [\mu_n(\mathbf{x}) n(\mathbf{x}) \nabla E_{F,n}(\mathbf{x})] \equiv G(\mathbf{x}) - R(\mathbf{x}) \quad (1.75)$$

and

$$\nabla \cdot \mathbf{j}_p(\mathbf{x}) = \nabla \cdot [\mu_p(\mathbf{x}) p(\mathbf{x}) \nabla E_{F,p}(\mathbf{x})] \equiv G(\mathbf{x}) - R(\mathbf{x}) \quad (1.76)$$

two boundary value problems for the Fermi levels $E_{F,n}(\mathbf{x})$ and $E_{F,p}(\mathbf{x})$. These two equations now need to be solved self-consistently with the nonlinear Poisson equation (1.46)

$$\nabla \cdot (\epsilon \nabla \phi) = -e (p - n + N_D^+[\phi] - N_A^-[\phi] + \rho_s) \quad (1.77)$$

in order to obtain the final quantum-corrected carrier densities and currents. See for example [19] for simulation results that have obtained in this fashion for a double-gate MOSFET similar to the one shown in Fig.1.1.

1.4.5 Quantum ballistic transport

Finally, a full quantum transport calculation can also be avoided if the semiconductor structure is small enough or the temperature low enough that no phonon scattering occurs and transport is fully ballistic in the absence of impurities. This situation occurs for instance in quantum interference devices [1] or also in quantum resonant tunneling structures [20] like the one shown in Fig. 1.7.

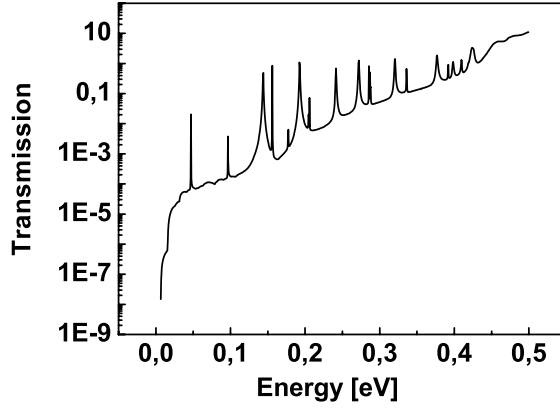


Fig. 1.8. The transmission function for the resonant tunneling structure shown in Fig. 1.7 (after [20]).

For these systems, we can use the Landau-Büttiker formalism [21, 22] to calculate the ballistic current $J_{\lambda\lambda'}$ between all contacts λ and λ' with the Landauer formula. This formula generally involves an integration over all quantum numbers that characterize the lead states and is given its most general form in [23]. Showing only the energy dependence in the integral for simplicity, we get here for the ballistic current

$$J_{\lambda\lambda'} = \frac{e}{\pi\hbar} \int dE T_{\lambda\lambda'}(E) [f_{\lambda}(E) - f_{\lambda'}(E)] \quad (1.78)$$

where E is the energy, $f_{\lambda}(E)$ the equilibrium distribution function inside contact λ , and $T_{\lambda\lambda'}(E)$ the transmission function between contact λ and λ' .

These transmission functions are then defined using the retarded single particle Green's function (see again [15])

$$\hat{G}^R(E) = \frac{1}{E - \hat{H} + i\eta} \quad (1.79)$$

as

$$T_{\lambda\lambda'} = \text{Tr} \left(\hat{\Gamma}_{\lambda} \hat{G}^R \hat{\Gamma}_{\lambda'} \hat{G}^{R\dagger} \right), \quad \lambda \neq \lambda' \quad (1.80)$$

where the operators $\hat{\Gamma}_{\lambda}$ are related to the self-energy matrices $\hat{\Sigma}_{\lambda}$ in the contacts as

$$\hat{\Gamma}_{\lambda} = i \left(\hat{\Sigma}_{\lambda} - \hat{\Sigma}_{\lambda}^{\dagger} \right) \quad (1.81)$$

Since we have ballistic transport both inside of the device and also in the contact regions, scattering only occurs at the contact-device boundaries and $\hat{\Sigma}_{\lambda}$ disappears everywhere else. This then allows us to use the contact block reduction method [24] for determining $T_{\lambda\lambda'}$ (see Fig. 1.8).

1.5 The nextnano³ simulation package

1.5.1 Capabilities overview

Most of the physical models that we have discussed so far have been implemented into **nextnano³**, a software package that the authors have specifically designed for the simulation of realistic nanoscale heterostructures in one, two, and three dimensions [3, 18]. In specific, the electronic structure is calculated by solving self-consistently the coupled system of the nonlinear Poisson equation (1.77) and Schrödinger's equation. For the Schrödinger's equation, we use either the effective mass approximation for the electrons (1.18) and the 6-band k-p-approximation for the holes (1.22), or an 8-band k-p-approximation for both electrons and holes at the same time.

In addition, we also perform strain relaxation in order to determine the strain tensor $\varepsilon_{ij}(\mathbf{x})$ and the strain-dependent changes in the conduction (1.31) and valence band (1.33). The presence of strain-induced piezoelectric charges and the effects of the spin-orbit interaction on the valence bands can be taken into account as well.

Furthermore, the quantum-corrected drift-diffusion equations (1.75-1.76) described above have been implemented to allow the determination of quasi-Fermi levels and particle currents for large classical devices and also many mesoscopic quantum structures. In addition, various phenomenological models for mobility, generation, and recombination are available in order to obtain more accurate simulation results.

The parameters entering these models and describing the material properties of various semiconductors and semiconductor alloys are automatically read in from a large materials database that can also be modified and extended by the software user. Similarly, a description of the device geometry, doping and alloy profiles, and simulation options is read from an external input file that can be easily modified by the user as well.

1.5.2 Numerical methods

The numerical methods used in **nextnano³** follow from the simple fact that the equations we need to solve are sets of coupled partial differential equations (PDEs) in position space. This immediately necessitates their discretization on a grid. In order to achieve a highly efficient but also simple software implementation only nonuniform tensor grids are used. The mapping of the PDEs onto the grid is achieved using box discretization, since this discretization scheme is flux conserving in the presence of material discontinuities as they naturally occur in the simulation of heterostructures.

As a result of this discretization procedure, every differential operator in these PDEs now becomes a sparse $N \times N$ -matrix, where N is the number of nodes in the grid. This number of grid nodes now scales as

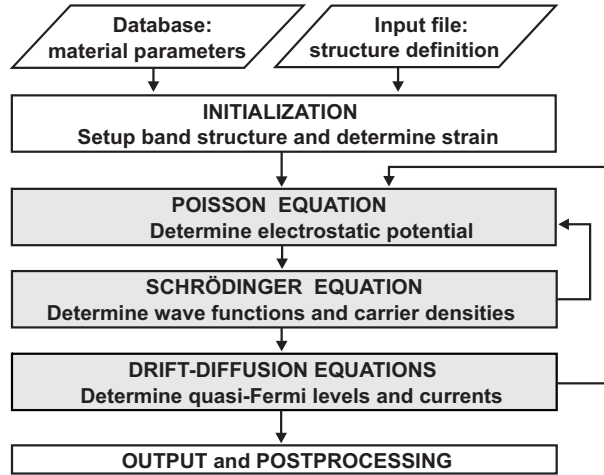


Fig. 1.9. An overview of the program flow in **nextnano**³.

$$N \sim \frac{1}{(\Delta x)^D} \quad (1.82)$$

where Δx is the desired space accuracy and D the number of space dimensions. Here we see immediately that three-dimensional simulations require extremely large matrices that cannot be easily stored and processed, unlike one explicitly exploits the sparsity structure of the matrices with its many vanishing entries. Similarly, every rank- r function over real space becomes after discretization an rN -dimensional vector, with $r = 1$ for scalar function like the electrostatic potential or the quasi-Fermi levels, $r = D$ for vector-valued functions like the particle currents, and $r = D^2$ for rank-2 tensor fields like the strain tensor.

Therefore, every PDE that is a boundary value problem (like the Poisson or the stationary drift-diffusion equation) becomes after discretization a large system of linear or nonlinear equations (N equations and unknowns), while the Schrödinger equation as an operator eigenvalue problem becomes a similarly large matrix eigenvalue problem with discretized wave functions as eigenvectors. Due to the sparsity of the underlying system matrices, these large matrix problems can now be efficiently solved using specialized linear algebra routines for sparse matrices like the conjugate gradient method or the Arnoldi iteration (see [25] for an in-depth presentation).

In addition, standard algorithms like the Newton method with line search are used to deal with nonlinearity like in Poisson's equation, while elaborate iteration schemes like the predictor-corrector approach [26] are employed in order to avoid numerical instabilities in finding a self-consistent solution. As recapitulation, an overview of the program flow in **nextnano**³ is also shown in Fig. 1.9.

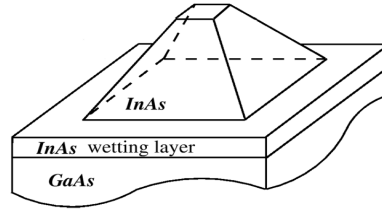


Fig. 1.10. A schematic plot of a self-assembled quantum dot.

1.5.3 Example application

As example application for the use of **nextnano**³, we simulate the mechanical and electronic properties of self-assembled quantum dots. Optoelectronic devices based on quantum dots have already demonstrated superior characteristics compared to conventional systems that give rise to the expectation that quantum dot lasers and modulators will be widely used in the future. Furthermore, quantum dots are also supposed to be the main elements in single-electron systems needed for quantum computing.

For this reason, there is a lot of interest in the study of quantum dots, as for instance self-assembled dots as the one shown in Fig. 1.10. This specific type of dot is high strained due to the lattice mismatch between InAs dot and GaAs substrate which gives rise to a large piezoelectric charge. Since these piezoelectric charges also modify the electrostatic potential that is felt by electrons or holes bound in the dot, we can expect that the shape of the electron and hole wave function is strongly influenced by the strain.

Using **nextnano**³, M. Povolotskyi et al. [27] have calculated the strain and the piezoelectric charge for a pyramidal quantum dot as shown in Fig. 1.10. Their results for a dot grown on a (311)-GaAs substrate is shown in Figs. 1.11 and 1.12. Here it is most noteworthy that the strain distribution and therefore also the piezoelectric charge is not symmetric despite the symmetric dot shape. As an immediate result, the electrostatic potential and therefore eventually also the electron and hole wave functions will not be symmetric. This asymmetry can have a huge influence on the overlap of electron and hole wave functions and therefore also on the dot's exciton absorption, which is crucial for the dot's optoelectronic performance.

References

1. M. Sabathil, D. Mamaluy, P. Vogl: *Semicond. Sci. Technol.* **19**, S137 (2004)
2. P.Y.Yu, M. Cardona: *Fundamentals of Semiconductors* (Springer, Berlin Heidelberg New York 1996)

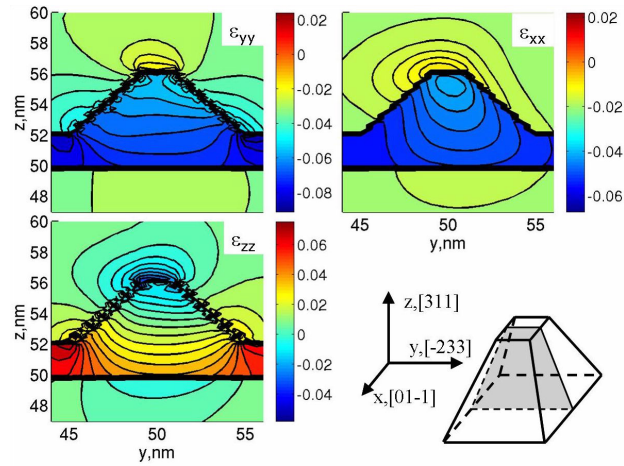


Fig. 1.11. Components of the strain tensor for a quantum dot with a composition and geometry as shown in Fig. 1.10. The dot is assumed to have grown on a (311)-substrate (after [27]).

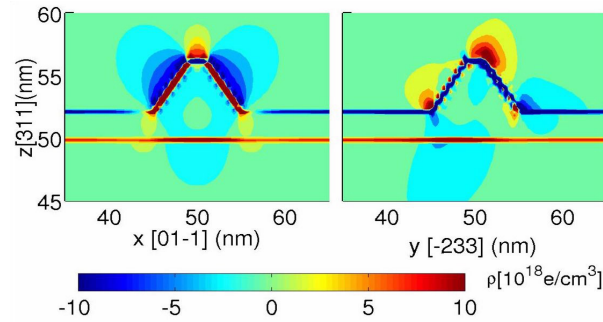


Fig. 1.12. The piezoelectric charge that is induced by the strain shown in Fig. 1.11 (after [27]).

3. The **nextnano**³ simulation package and example input files can be downloaded from <http://www.wsi.tum.de/nextnano3/>.
4. J.A. Majewski, A. Trellakis, P. Vogl et al: *physica status solidi (c)* **1**, 2003 (2004)
5. P. Löwdin: *J. Chem. Phys.* **19**, 1396 (1951)
6. J.M. Luttinger, W. Kohn: *Phys. Rev.* **97**, 869 (1955)
7. G. Dresselhaus, A.F. Kip, C. Kittel: *Phys. Rev.* **98**, 368 (1955)
8. C.R. Pidgeon, R. N. Brown: *Phys. Rev.* **146**, 575 (1966)
9. G. Bastard: *Phys. Rev. B* **24**, 5693 (1981)
10. E.O. Kane: The k-p method. In: *Semiconductors and Semimetals: III-V compounds*, vol. 1, ed by R.K. Willardson, A.C. Beer (Academic Press, New York 1966) pp. 75-100

11. M.G. Burt: J. Phys.: Condens. Matter **4**, 6651 (1992)
12. M.G. Burt: J. Phys.: Condens. Matter **11**, R53 (1999)
13. T.B. Bahder: Phys. Rev. B **41**, 11992 (1990)
14. R. Lake et al: J. Appl. Phys. **81**, 7845 (1997)
15. S. Datta: *Electronic Transport in Mesoscopic Systems*, (Cambridge University Press, Cambridge 1997)
16. D.K. Ferry, S.M. Goodnick: *Transport in Nanostructures*, (Cambridge University Press, Cambridge 2000)
17. S. Hackenbuchner: Elektronische Struktur von Halbleiter-Nanobau-elementen im thermodynamischen Nichtgleichgewicht. Ph.D. Thesis, TU München, München (2002)
18. M. Sabathil, S. Hackenbuchner, P. Vogl et al: J. Comp. Electronics **1**, 81 (2002)
19. K. Kim, O. Kwon, A. Trellakis et al.: J. Korean Phys. Soc. **45**, S909 (2004)
20. M. Sabathil, S. Birner, P.Vogl et al: J. Comp. Electronics **2**, 269 (2003)
21. R. Landauer: Phys. Scr., T **42**, 110 (1992).
22. M. Büttiker: IBM J. Res. Dev. **32**, 317 (1988)
23. A. Di Carlo, P. Vogl: Phys. Rev. B **50**, 8358 (1994)
24. D. Mamaluy, M. Sabathil, P. Vogl: Phys. Rev. B **93**, 4628 (2003)
25. L. N. Trefethen, D. Bau III: *Numerical Linear Algebra*, (SIAM Society for Industrial & Applied Mathematics, Philadelphia 1997)
26. A. Trellakis et al: J. Appl. Phys. **81** 7880 (1997)
27. M. Povolotskyi, A. Di Carlo, P. Vogl et al: IEEE Trans. Nanotechnol. **3**, 124 (2004)